Supporting Information

Characterizing the MnO_2 dissolution process via EQCM for rechargeable aqueous batteries

Minseok Choi[1*], Aaron Reed[1*], Cyrus Mirsafian[1], Sangha Baek[2], Randy Chen[1], and Bruce Dunn[1]

1. Henry Samueli School of Engineering, Materials Science and Engineering Department, University of California, Los Angeles, CA 90095, USA
2. School of Chemical Engineering, Sungkyunkwan University, Suwon-si, Gyeonggi-do, 16419, Republic of Korea

*These authors contributed equally: Minseok Choi, Aaron Reed

1. Materials

Electrolytes

Table S1. Electrolyte composition and measured pH.

Electrolyte	Measured pH
1M $MnSO_4$ + 0.1M H_2SO_4	0.81-1
1M $MnSO_4$ + 0.03M H_2SO_4	1.5-1.8
1M $MnSO_4$ + 0.01M H_2SO_4	2-2.3
1M $MnSO_4$	3-3.2
1M $MnSO_4$ + 15mM NaOH	4.11
1M $MnSO_4$ + 19mM NaOH	5.4

2. Characterization

Material Characterization

Electrochemical measurements were made using the Biologic VMP 3 multichannel Potentiostat. For UV-vis spectroscopy, measurements were taken with a Cary 60 UV-Vis Spectrometer from Agilent Technologies. X-ray diffraction (XRD) patterns were collected on a Malvern Panalytical X'Pert PRO (Cu Kα radiation, λ=1.54 Å) at room temperature. X-ray photoelectron spectroscopy was performed using a Kratos Axis Ultra XPS and used a monochromatic aluminum X-ray source voltage of 12 kV and emission current of 10 mA.

EQCM background

The electrochemical quartz crystal microbalance (EQCM) is an *operando* analytical technique that enables simultaneous measurement of electrochemical response and the mass change during redox reactions. It combines the sensitivity of a quartz crystal microbalance with the control of an electrochemical cell, allowing direct correlation between charge transfer and interfacial mass variation in real time.

In a typical EQCM setup, a gold-coated quartz crystal sensor serves as the working electrode. This sensor simultaneously functions as an electrochemical interface and a vibrational transducer. When an alternating potential is applied across the quartz crystal, it oscillates at a characteristic resonance frequency determined by its thickness and mass. Any change in the surface mass - arising from such processes as ion adsorption, desorption, or electrochemical dissolution/deposition - alters the resonance frequency. By monitoring this frequency shift as a function of applied potential, EQCM quantitatively tracks the dynamic mass change at the electrode–electrolyte interface.

The relationship between the frequency shift (Δf) and the mass change (Δm) is described by the Sauerbrey equation:

$$\Delta f = -\frac{2f_0^2}{\sqrt{\rho_q \mu_q}} \Delta m = -\frac{1}{C_f} \Delta m \qquad \text{(Eq. S1)}$$

where f_0 is the fundamental resonance frequency of the crystal, ρ_q is the density of quartz, and μ_q is the shear modulus of quartz. The conversion factor (C_f) was determined via the electrodeposition of copper from a $CuSO_4$ electrolyte. During deposition, simultaneous frequency shifts and electrochemical currents were recorded using the QCM and potentiostat, respectively. The deposited copper mass was quantified by integrating the current to obtain the total charge and converting it to moles of Cu via Faraday's law. Correlating the calculated copper mass with the measured frequency change (Δf, Hz) yielded a conversion factor of 76.2 Hz μg^{-1}.

This linear relationship holds when the interfacial layer behaves as a rigid film, as typically observed in inorganic systems such as MnO_2. In cases where the deposited or adsorbed layer exhibits viscoelastic properties—such as hydrated or polymeric films—frequency dissipation analysis or viscoelastic corrections (e.g., Voigt–Voinova model) can be applied. However, for rigid oxide electrodes in aqueous media, the Sauerbrey approximation provides accurate and reliable results.

Overall, EQCM serves as a powerful diagnostic tool for quantifying mass and charge coupling in real time. Its high mass sensitivity (on the order of nanograms per square centimeter) makes it particularly valuable for studying electrochemical reactions involving surface adsorption, ion exchange, and redox-driven dissolution in transition-metal oxide systems.

3. Calculation

Calculating formula mass (dm/dq)

To compare the theoretical mass change associated with each redox reaction, the expected mass variation was calculated using Faraday's law**:**

$$\frac{\Delta m}{\Delta Q} = \frac{M}{nF} \quad \text{(Eq. S2)}$$

where Δm is the mass change (g), ΔQ is the total charge transferred (C), *M* is the molar mass of the active species (g mol^{-1}), *n* is the number of electrons involved in the reaction, and *F* is the Faraday constant (96,485 C mol^{-1}).

Example Calculation for $Mn^{2+} \rightarrow$ MnOOH

$$\frac{\Delta m}{\Delta Q} = \frac{M}{nF} = \frac{87.94}{1\times96485} = 0.911 \text{mg C}^{-1} \quad \text{(Eq. S3)}$$

Table S2. Formula mass (dm/dq) for redox equations

Redox equation	dm/dq (mg C^{-1})
$Mn^{2+} \leftrightarrow MnOOH$	0.911
$MnOOH \leftrightarrow MnO_2$	0.010
$Mn^{3+} \leftrightarrow MnO_2$	0.901
$Mn^{2+} \leftrightarrow MnO_2$	0.450

The chemical dissolution of MnOOH to Mn^{3+} yields a dm/dq value of negative infinity because this process is non-faradaic and does not involve electron transfer. Consequently, the number of electrons exchanged (n) is zero. Substitution into Eq. S2 therefore results in an undefined (formally negative infinite) dm/dq value, reflecting mass loss in the absence of measurable charge transfer.

Calculating capacity losses

Chemical dissolution is considered as the amount of non-Faradaic mass loss associated with electrodeposited MnO_2. This occurs through Equation S4, where MnOOH is protonated to form soluble Mn^{3+}.

$$MnOOH + 3H^+ \leftrightarrow Mn^{3+} + 2H_2O \quad \text{(Eq. S4)}$$

On the EQCM, this mass must be decoupled from other non-Faradaic mass losses such as desorption and chemical dissolution of mass deposited at open circuit (OCV). A representative calculation is summarized in Table S3 for a 2.37 pH electrolyte of 1M $MnSO_4$ + 0.01M H_2SO_4. First, the total non-Faradaic mass loss is calculated by integrating the dm/dq plot under the theoretical dm/dq for MnO_2 to Mn^{2+} (-0.45 mg/C). This value is defined as the total amount of non-Faradaic mass loss occurring during discharge, which includes desorption of adsorbed species, chemical dissolution of OCV deposited mass, and chemical dissolution of electrodeposited MnO_2. The amount of chemical dissolution of electrodeposited mass is then calculated by subtracting the desorption mass and the mass from chemical dissolution of OCV deposited species. The resulting value is then equal to the mass loss contributing to capacity loss. This mass can then be converted back to capacity by dividing by the theoretical dm/dq for MnOOH to Mn^{2+}. The capacity loss from leftover mass can be calculated in a similar way. In this case, leftover mass is simply taken as the remaining mass on the EQCM sensor after reaching the 0 V cutoff potential. This mass is then converted to capacity by dividing by the theoretical dm/dq for MnO_2 to Mn^{2+}, where the conversion assumes all leftover mass is MnO_2.

Lastly, the total capacity loss is taken as the sum of capacity losses from chemical dissolution and incomplete dissolution, and the coulombic efficiency is calculated with a charge capacity of 37 μAh. As shown in Table S3, the coulombic efficiency calculated from EQCM matches closely with the electrochemically measured value. Calculating the coulombic efficiency for each cycle, the deposition capacity was extracted by isolating the faradaic MnO_2 deposition component, excluding contributions from the oxygen evolution reaction and double-layer capacitance (see Figure S10 for details).[1]

Table S3. Example calculation of capacity losses for a pH 2.37 electrolyte during a 5 μA discharge

Process	**Calculated Mass (μg)**
Total Non-Faradaic Mass Loss	32.2
Adsorbed Mass	11.5
OCV Deposited Mass	12.3
Chemical Dissolution Mass	8.4
Associated Capacity Loss	**2.56 μAh**
Leftover Mass	2.2
Associated Capacity Loss	**1.36 μAh**

Total Capacity Loss	**3.92 μAh**
Coulombic Efficiency	**89.4%**
Measured Coulombic Efficiency	**89.6%**

4. Supplementary Figures

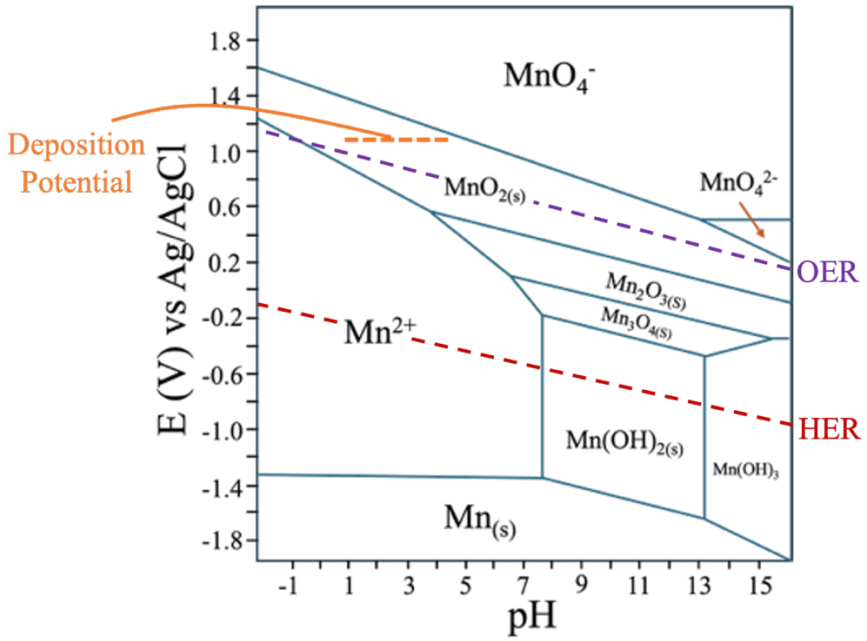

Figure S1. Pourbaix diagram of MnO_2

Note: Orange line is the deposition potential used experimentally for electrolytes with various pH (from pH 1 to pH 5). Although the applied deposition potential is slightly above the thermodynamic onset of the oxygen evolution reaction (OER), MnO_2 deposition competes with OER for anodic current. The rapid proton-coupled oxidation of Mn^{2+} to MnO_2 preferentially consumes charge, kinetically suppressing and minimizing OER.

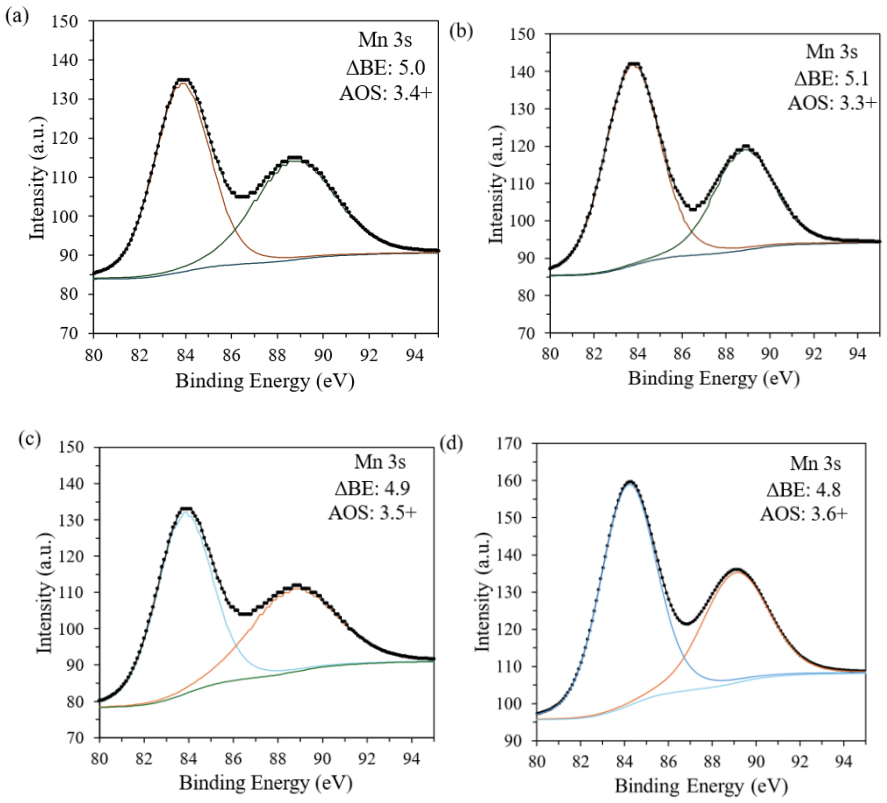

Figure S2. XPS Scan of MnO_2 deposited in 1 pH a) with OCV and b) without OCV, and 5.4 pH c) with OCV and d) without OCV

Note: There are two peak contributions to the Mn 3s spectra. This arises because non-ionized 3s electrons couple to the unpaired valence band electrons in the 3d orbitals. Should the spins couple in a parallel fashion, a lower binding energy results while coupling in an anti-parallel manner leads to a higher binding energy. Thus, two peaks result in the Mn 3s spectra. The oxidation state of the Mn is dependent on the number of valence electrons in the 3d orbital and therefore impacts the energy difference of the two peaks. A peak separation (difference in band energy, ΔBE) of 4.4 eV corresponds to the 4+ average oxidation state (AOS) while a peak separation of 5.4 eV corresponds to the 3+ average oxidation state.[2] Thus, the peak separation obtained experimentally was used to determine the average oxidation state of the sample. The AOS of electrodeposited MnO_x with no OCV has a small dependence on pH, with higher pH electrolytes favoring a more oxidized manganese product, and lower pH electrolytes favoring a more reduced manganese product. Conversely, the OCV deposited mass is relatively independent of electrolyte pH, showing an oxidation state of 3.4-3.5+ in both cases. These results demonstrate that the average oxidation state of Mn in the overpotential-deposited layer is less strongly governed by electrolyte pH compared to the electrochemically deposited layer.

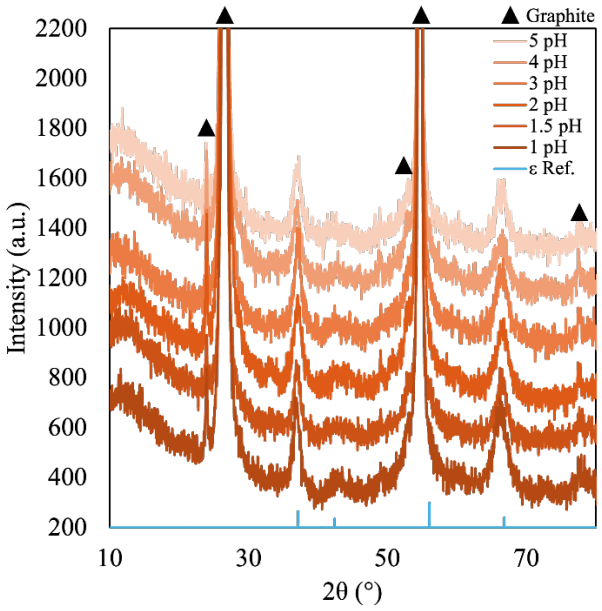

Figure S3. XRD pattern of electrodeposited MnO_2 on a graphite foil

Note: The electrodeposited MnO_2 film is nanocrystalline and thinner than the penetration depth of the Cu Kα X-ray radiation. As a result of, most of the peaks originate from the graphite foil substrate. The two MnO_2 peaks that can be clearly distinguished at 37° and 67° 2θ are indexed to the (100) and (110) peaks of ε-MnO_2, respectively.

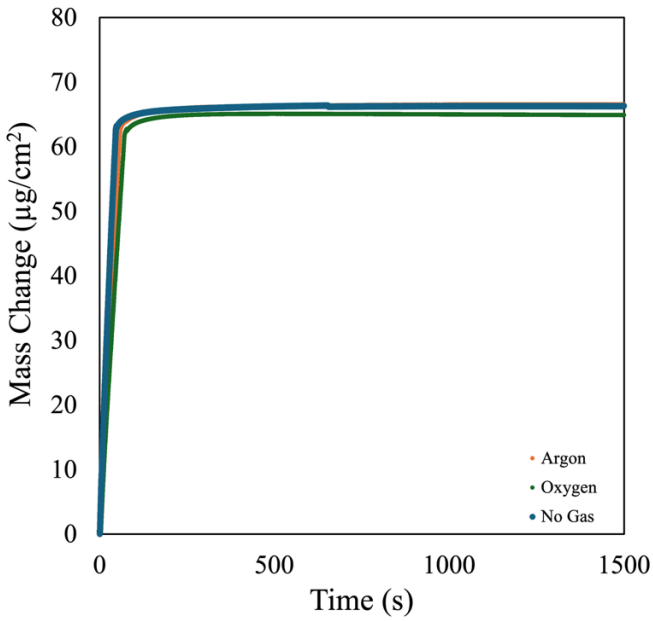

Figure S4. Deposition mass change comparison between as is, ultra-high purity (UHP) argon and oxygen treatment

Note: Ultra-high-purity (UHP) argon and oxygen were bubbled through the pH 1.5 electrolyte for 30 min prior to electrochemical testing to assess whether dissolved oxygen acts as the oxidizing agent responsible for overpotential-driven deposition. No discernible differences were observed between argon-purged, oxygen-saturated, and untreated electrolytes, indicating that the dissolved oxygen concentration does not influence the overpotential deposition behavior. These results therefore exclude oxygen as the primary oxidizing agent in this process.

Mass increase due to an adsorption phenomenon

In the third stage of the dissolution process, a mass increase of approximately 4 μg was observed, and the measured apparent dm/dq at this stage reached nearly 0.5 mg C^{-1}. This value significantly exceeds the theoretical dm/dq expected from any faradaic reaction in this system. One possible explanation for this unusually mass gain is the physisorption of solvated species onto the MnO_2 surface.[3]

Two pieces of evidence support this hypothesis. First, the series resonance frequency (f_s) and parallel resonance frequency (f_p) of the QCM response begin to deviate from each other during this stage. As shown in Figure S5, around 19150s, fs (in black) decreases while f_p (in red) continues to increase, leading to a noticeable frequency separation. This divergence indicates that both mass loading and viscoelastic changes occur simultaneously within the MnO_2 film.[4]

Such viscoelastic behavior can arise from the presence of physiosorbed or loosely bound species at the electrode–electrolyte interface. Because these adsorbed layers are mechanically softer than the underlying MnO_2 film, they do not move perfectly in phase with the oscillating crystal.[5,6] This lag in motion introduces energy dissipation within the system, which is manifested as the separation between f_s and f_p in the frequency response.[7]

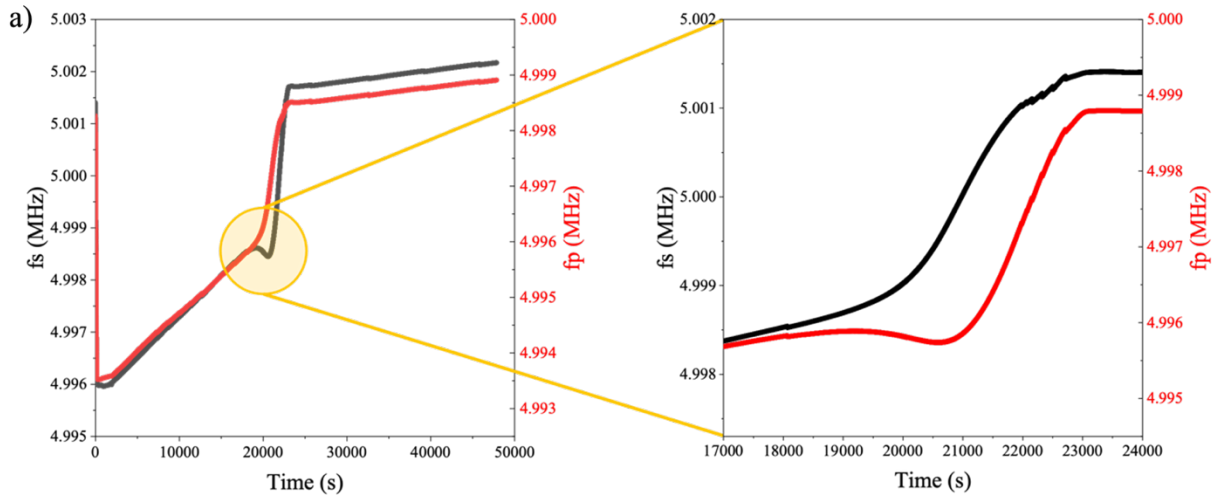

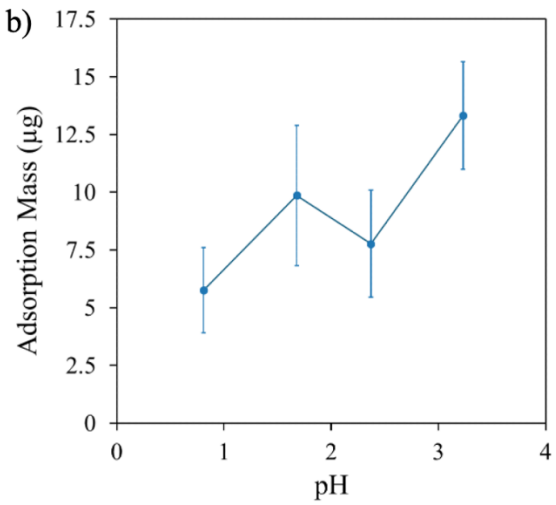

Figure S5. Mass increase during dissolution; a) Series frequency (f_s) and parallel frequency (f_p) changes during the dissolution process in pH 1.5 electrolyte. b) Average adsorption at different electrolyte pH levels

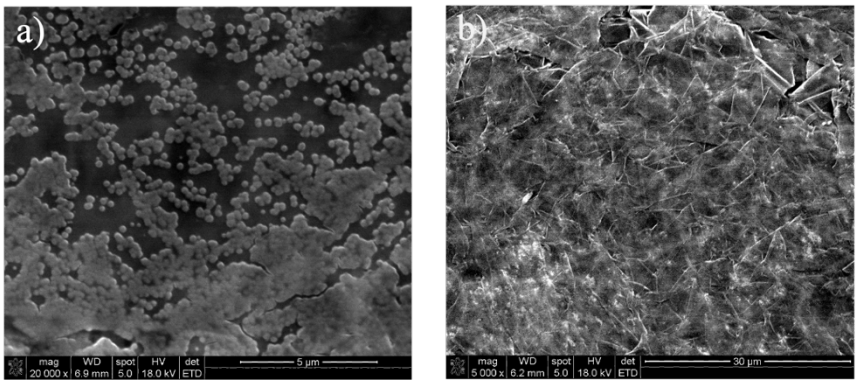

Figure S6. SEM image of graphite foil after a) 50% of dissolution and b) 100% dissolution in pH 1 electrolyte

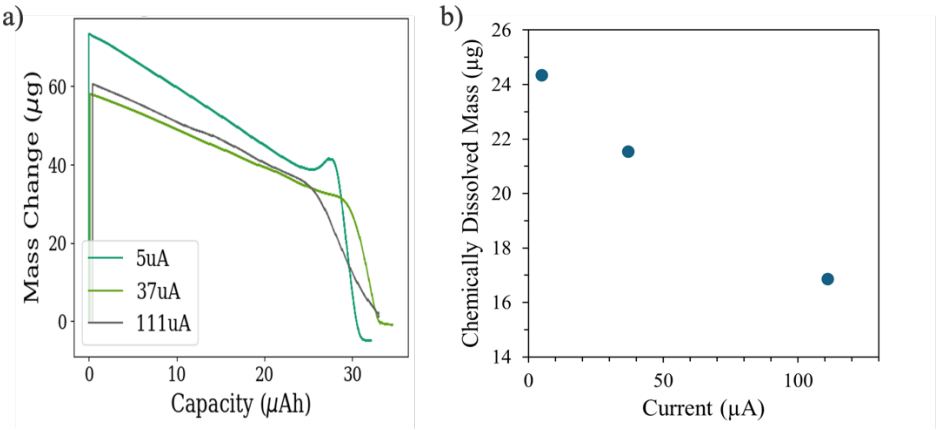

Figure S7. Effect of dissolution current on mass change at pH 1; a) Mass change of MnO_2 in different currents in pH 1 electrolyte. The effective electrode area is 1 cm^2. b) Amount of chemical dissolution at various current rates

Note: The dependence of dissolution behavior on current was investigated at pH 1 for a range of values including C/7, 1C and 3C (current rates of 5, 37, and 111μA, respectively) as shown in Figure S7. The electrochemical dissolution slopes remain very similar for the different currents, suggesting the current rate does not impact the nature of the electrochemical dissolution. Moreover, the capacity for different rates was 33±1 μAh from 5 to 111μA cm. (Figure 7a). One feature which does change is the amount of chemical dissolution which decreases as current rate increases (Figure 7b). The current rate, however, may just be one important variable as chemical dissolution also may be dependent on the kinetics of chemical dissolution. In that case, the length of time in the electrolyte will affect the chemical dissolution. It is evident that additional experiments aimed at unraveling these two effects are needed.

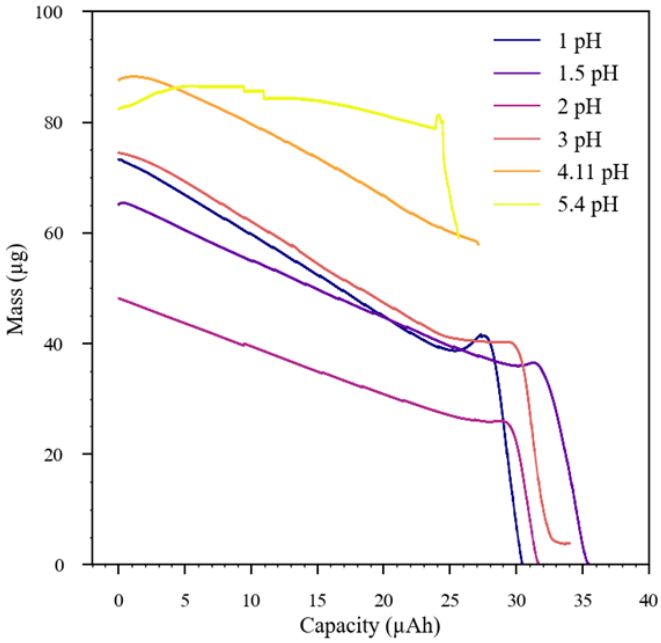

Figure S8. Mass change during the dissolution vs discharge capacity of MnO_2 in various pH electrolytes

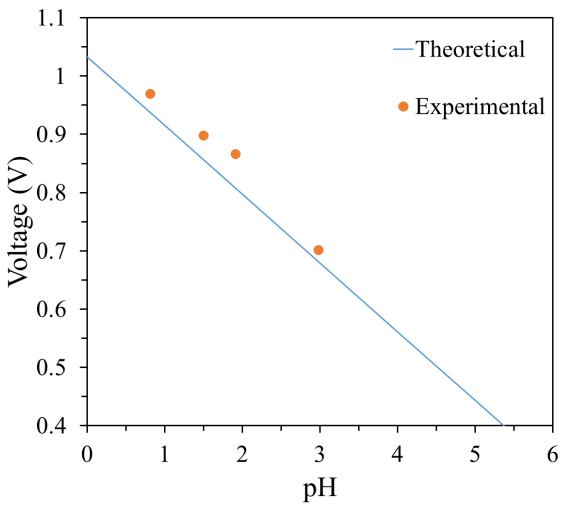

Figure S9. Comparison between theoretical (blue line) and experimental (orange dot) onset MnO_2 deposition potential plateau at different pH level

Note: The theoretical value was calculated by using Nernstian relationship

$$E' = E^0 + \frac{RT}{nF} ln \frac{[H^+]^4}{[Mn^{2+}]} = E^0 - 0.12 * pH \qquad \text{(Eq. S4)}$$

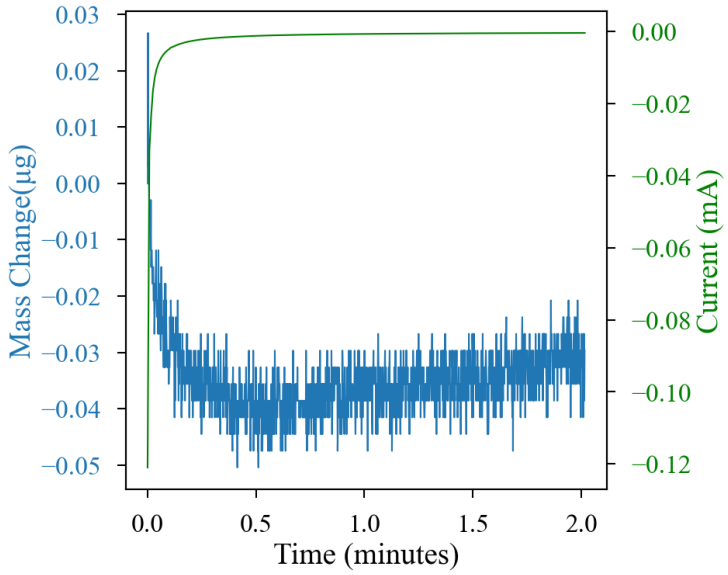

Figure S10. Mass change (µg) and current (mA) during double layer formation on the EQCM Au sensor. The measurement was conducted in 1M $MnSO_4$ at a constant voltage of 0.5V vs Ag/AgCl with a Pt counter electrode and an Ag/AgCl reference electrode.

Note: To assess the influence of double layer formation on deposition, we applied an initial voltage of 0.5V vs Ag/AgCl for 2 minutes prior to stepping the voltage up to 1.1V vs Ag/AgCl for MnO_2 electrodeposition in the EQCM setup. During this initial voltage hold, the double layer forms and there is 0.07 µAh of capacity passed along with 0.04 µg of mass change. This accounts for a small percentage (0.19%) of the total deposition capacity and (0.053%) of the total deposition mass, so it is ignored in subsequent calculations.

References

(1) Li, J.; Li, C.; Liu, B.; Li, Y.; Borodin, O.; Nazar, L. F. Aqueous Eutectic Electrolytes Suppress Oxygen and Hydrogen Evolution for Long-Life Zn||MnO2 Dual-Electrode-Free Batteries. *Nat. Energy* **2026**. https://doi.org/10.1038/s41560-025-01958-8.

(2) Ilton, E. S.; Post, J. E.; Heaney, P. J.; Ling, F. T.; Kerisit, S. N. XPS Determination of Mn Oxidation States in Mn (Hydr)Oxides. *Appl. Surf. Sci.* **2016**, *366*, 475–485. https://doi.org/10.1016/j.apsusc.2015.12.159.

(3) Johannsmann, D.; Langhoff, A.; Leppin, C. Studying Soft Interfaces with Shear Waves: Principles and Applications of the Quartz Crystal Microbalance (QCM). *Sensors* **2021**, *21* (10), 3490. https://doi.org/10.3390/s21103490.

(4) Gopalakrishna, S.; Langhoff, A.; Brenner, G.; Johannsmann, D. Soft Viscoelastic Particles in Contact with a Quartz Crystal Microbalance (QCM): A Frequency-Domain Lattice Boltzmann Simulation. *Anal. Chem.* **2021**, *93* (29), 10229–10235. https://doi.org/10.1021/acs.analchem.1c01612.

(5) Buttry, D. A.; Ward, M. D. Measurement of Interfacial Processes at Electrode Surfaces with the Electrochemical Quartz Crystal Microbalance. *Chem. Rev.* **1992**, *92* (6), 1355–1379. https://doi.org/10.1021/cr00014a006.

(6) Cho, N.-J.; Frank, C. W.; Kasemo, B.; Höök, F. Quartz Crystal Microbalance with Dissipation Monitoring of Supported Lipid Bilayers on Various Substrates. *Nat. Protoc.* **2010**, *5* (6), 1096–1106. https://doi.org/10.1038/nprot.2010.65.

(7) Aurbach, D.; Zaban, A. The Application of EQCM to the Study of the Electrochemical Behavior of Propylene Carbonate Solutions. *J. Electroanal. Chem.* **1995**, *393* (1–2), 43–53. https://doi.org/10.1016/0022-0728(95)04014-F.